WILEY | Hindawi

Research Article

Impact of Single and Combined Faults Composed of Rotor Eccentricity and Stator Interturn Short Circuit on Electromagnetic Torque Ripples in Synchronous Generator

Yu-Ling He [iD],[1] **Zhi-Jie Zhang,**[1] **Xiao-Long Wang** [iD],[1] **Peng Gao,**[2] **David Gerada,**[3] **Chris Gerada,**[3] **and Gaurang Vakil**[3]

[1]*Department of Mechanical Engineering, North China Electric Power University, Baoding 071003, Hebei, China*
[2]*School of Electrical and Information Engineering, Tianjin University, Tianjin 300072, China*
[3]*Department of Electrical and Electronic Engineering, University of Nottingham, University Park, Nottingham, NG7 2RD, UK*

Correspondence should be addressed to Xiao-Long Wang; wangxiaolong0312@126.com

In order to comprehensively study and identify the electromagnetic torque (EMT) difference among the single static air-gap eccentricity (SAGE) fault, the single stator interturn short circuit fault (SISC), and the combined fault composed of these two, this article investigates the EMT ripple properties due to the mentioned three faults. Different from other studies, this paper considers not only the effect of the single fault types but also the impact of the single fault combinations on the EMT ripple characteristics. Detailed EMT expressions for each fault are firstly derived on the basis of the magnetic flux density (MFD) analysis. Then, finite element calculation and experimental study on a CS-5 prototype generator with two poles at 3000 rpm, which is specifically designed and manufactured ourselves, are carried out to validate the analysis result. It is found that the three faults will induce different ripple components in EMT. The combined faults have the most intensive impact sensitivity on the EMT ripples, while the single SAGE fault ranks the last in the impact effect.

1. Introduction

In synchronous generators, the electromagnetic torque (EMT) ripple is a primary parameter for the energy conversion. Under the stable running conditions, the input mechanical moment should be equivalent to the electromagnetic torque (ignoring the energy loss). Since EMT is the resisting moment, its ripple properties are closely related to the output stability of the generator. On the one hand, large EMT ripples will lead to the overfrequent adjustment of the automatic control system to modify the input mechanical moment, and obviously this is harmful for the generator set [1]. On the other hand, intensive EMT ripples will cause the torsional vibration of the shaft and may lead to the fatigue of the shaft material after a long-term performance [2]. More seriously, it may even lead to a disaster [3].

By far, the EMT ripple properties in normal condition have been well studied by scholars [4, 5]. Since the magnetic flux density (MFD), which is closely related to EMT, will be changed due to different faults, the EMT ripple characteristics will be also varied in different fault cases. For instance, Hao et al. found that the occurrence of rotor interturn short circuit will increase each odd and even harmonic of EMT [6]. In the meantime, Song et al. found that the segmented armature winding can effectively restrain the torque ripples under the stator short circuit fault [7]. However, the EMT properties due to varied faults, especially the combined faults such as the static air-gap eccentricity (SAGE) and stator interturn short circuit (SISC) composite fault, have not been fully studied.

For SAGE, scholars have investigated both the mechanical and the electrical faulty properties. For instance, He et al. investigated the unbalanced magnetic pull (UMP) [8], the vibration characteristics of the rotor [9], and the circulating current inside the parallel branches [10]. Besides the mechanical characteristics, it is also found that the stator

phase current is an effective tool to identify the broken magnet and SAGE in permanent magnet synchronous motors [11], while at the same time, the shaft voltage measurements have been found as a better means for the optimal measurement modality that leads to a minimal identification error of SAGE in synchronous machines [12]. Meanwhile, a method to quantify the rotor eccentricities in synchronous machines by exploiting the unbalance caused in the split-phase currents was proposed by Bruzzese [13]. Also, an alternative method based on the analysis of line neutral voltage taking place between the supply and the stator neutrals in induction motor was presented by Oumaamar et al. [14].

For SISC, Nadarajan et al. presented a hybrid approach to set up the synchronous generator by combining the dq0 modeling with the winding function [15]. This approach improves the accuracy and reduces the modeling complexity. In addition, Moon et al. proposed a method that uses voltage and current residual components to diagnose the exact phase and the severity of SISC in permanent-magnet synchronous machine [16]. It is found that the occurrence of SISC will significantly impact on the zero-sequence current [17], the negative-sequence current [18], the whole stator current [19], the rotor current [20], and the electromagnetic torque [21].

The above studies employed different parameters to describe the fault characteristics for either the SAGE fault or the SISC fault, while few of them have paid attention to the combined faults composed of these two. However, the actual operating conditions can be far more complicated than just one single fault. A generator may have two different faults at the same time [22]. It is found that the faulty characteristics under the composite fault are different from the composed single faults [23]. Then, the following key point is how to distinguish the single and the combined faults by proper faulty characteristics.

In this paper, we proposed a comprehensive study on the impact of the single and the combined faults which are composed by SAGE and SISC on the electromagnetic torque ripples. The remainder of this paper is constructed as follows. The theoretical analysis model is derived in Section 2, while the FEA calculation and the experimental study are presented in Section 3. Finally, the primary conclusions from the investigation of this paper are drawn in Section 4.

2. Theoretical Analysis Model

2.1. Effect of SISC on MMF. The magnetomotive force (MMF) and the permeance per unit area (PPUA) are the basic parameters for calculating the EMT of the generator. Their values are directly dependent on the operating state of the generator. Once the SISC fault occurs, the MMF will be changed immediately. According to [23], the normal MMF can be written as

$$f(\alpha_m, t) = F_r \cos\left(\omega t - p\alpha_m + \psi + \frac{\pi}{2}\right) + F_s \cos(\omega t - p\alpha_m), \tag{1}$$

where F_s and F_r are the stator MMF and the rotor MMF, respectively, α_m is the mechanical angle to indicate the circumferential position of the air gap, and ψ is the internal power angle of generator.

When SISC takes place, as shown in Figure 1, the additional circulating current in the short circuit ring will produce a pulsating magnetic field which centers on the short circuit winding axis. This new magnetic field has the same frequency as the short circuit current, namely, 50 HZ. It can be expressed as

$$\begin{aligned} f_d(\alpha_m, t) &= F_d \cos\omega t \cos\alpha_m \\ &= F_{d+}\cos(\omega t + \alpha_m) + F_{d-}\cos(\omega t - \alpha_m), \end{aligned} \tag{2}$$

where F_{d+} and F_{d-} are the forwardly and the inversely rotating MMF amplitude, respectively, and $F_{d+} = F_{d-} = F_d/2$.

Since the rotating speed difference between the reversed MMF and the rotor is 2ω, an extra reversed electromotive force (EMF) at 2ω will be induced in the field windings. Then, the final excitation current in the field windings can be expressed as

$$I_f(t) = I_{f0} + I_{f2}\cos 2\omega t, \tag{3}$$

where I_{f0} is the DC component in the field windings produced by the exciting system, while I_{f2} is the current induced due to SISC.

Further, the air gap magnetic flux density (MFD) can be written as

$$B_m(t) = (I_{f0} + I_{f2}\cos 2\omega t)N\Lambda_0, \tag{4}$$

where N is the turn number of each pole and Λ_0 is the permeance of the air gap.

The EMFs of the three phases can be written as

$$\begin{cases} e_a(t) = (I_{f0} + I_{f2}\cos 2\omega t)KN\Lambda_0 \cos\omega t \\ = I_{f0}KN\Lambda_0 \cos\omega t + 0.5I_{f2}KN\Lambda_0 \cos\omega t + 0.5I_{f2}KN\Lambda_0 \cos 3\omega t, \\ e_b(t) = (I_{f0} + I_{f2}\cos 2\omega t)KN\Lambda_0 \cos(\omega t - 120°) \\ = I_{f0}KN\Lambda_0 \cos(\omega t - 120°) + 0.5I_{f2}KN\Lambda_0 \cos(\omega t + 120°) + 0.5I_{f2}KN\Lambda_0 \cos(3\omega t - 120°), \\ e_c(t) = (I_{f0} + I_{f2}\cos 2\omega t)KN\Lambda_0 \cos(\omega t + 120°) \\ = I_{f0}KN\Lambda_0 \cos(\omega t + 120°) + 0.5I_{f2}KN\Lambda_0 \cos(\omega t - 120°) + 0.5I_{f2}KN\Lambda_0 \cos(3\omega t + 120°), \end{cases} \tag{5}$$
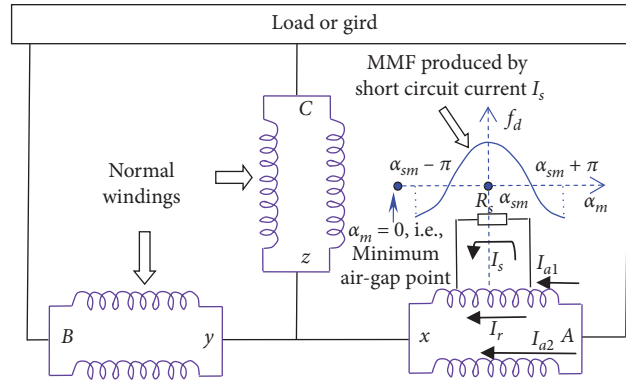
FIGURE 1: Diagrams of SISC.

where $K = 2qw_c k_{w1}\tau f L$, q is the slot number for each phase per pole, w_c is the turn number of each coil, k_{w1} is the fundamental winding factor, τ is the polar distance, f is the fundamental frequency, and L is the length of the stator core.

As indicated in (5), the induced EMF for each phase is composed of three parts. The first parts will form a forwardly rotating MMF at the fundamental frequency, since the phase angles for the three phases are 0, −120°, and +120°, respectively. On the contrary, the second parts will form a backwardly rotating MMF, while the third parts will form forwardly rotating MMF at 3ω. Consequently, the MMFs under SISC can be expressed as

$$f(\alpha_m, t) = \left(I_{f0} + I_{f2}\cos 2\omega t\right)N\cos\left(\omega t - p\alpha_m + \psi + \frac{\pi}{2}\right)$$
$$+ F_{s1+}\cos\left(\omega t - p\alpha_m\right) + F_{s1-}\cos\left(\omega t + p\alpha_m\right)$$
$$+ F_{s3+}\cos\left(3\omega t - p\alpha_m\right), \tag{6}$$

where F_{s1+} and F_{s3+} are the forwardly rotating MMFs of stator at ω and 3ω, respectively, F_{s1-} is the backwardly rotating MMF of stator at ω, and $F_{s3+} = F_{s1-}$. Expanding the first item in equation (6), the MMF under SISC can be modified to

$$f(\alpha_m, t) = F_{r1+}\cos\left(\omega t - p\alpha_m + \psi + \frac{\pi}{2}\right) + F_{s1+}\cos\left(\omega t - p\alpha_m\right)$$
$$+ F_{r1-}\cos\left(\omega t + p\alpha_m - \psi - \frac{\pi}{2}\right) + F_{s1-}\cos\left(\omega t + p\alpha_m\right)$$
$$+ F_{r3+}\cos\left(3\omega t - p\alpha_m + \psi + \frac{\pi}{2}\right) + F_{s3+}\cos\left(3\omega t - p\alpha_m\right), \tag{7}$$

where

$$F_{s3+} = F_{s1-}, F_{r1+} = NI_{f0}, F_{r1-} = F_{r3+} = 0.5NI_{f2}. \tag{8}$$

2.2. Impact of SAGE on PPUA.

SAGE will deform the air gap and further affect PPUA (see Figures 2(a) and 2(b)). According to Figure 2(b), $OB = R_s$, which is the inner radius of the stator core, and $O_1A = R_r$, which is the outer radius of the rotor core. The radial air-gap length can be written as

$$g(\alpha_m) = |\overline{OB}| - |\overline{OA}| = R_s - |\overline{OA}|, \tag{9}$$

where based on the cosine law it has

$$R_r^2 = |\overline{OA}|^2 + \left(g_0\delta_s\right)^2 - 2|\overline{OA}|g_0\delta_s\cos\alpha_m, \tag{10}$$

which can be further modified as

$$|\overline{OA}| = \frac{2g_0\delta_s\cos\alpha_m \pm \sqrt{\left(2g_0\delta_s\cos\alpha_m\right)^2 - 4\left(g_0^2\delta_s^2 - R_r^2\right)}}{2}$$
$$= g_0\delta_s\cos\alpha_m \pm \sqrt{\left(g_0\delta_s\cos\alpha_m\right)^2 - g_0^2\delta_s^2 + R_r^2}, \tag{11}$$

where g_0 is the average value of the radial air-gap length and δ_s is the relative SAGE in the radial direction. Then, the radial air-gap length can be obtained as

$$g(\alpha_m) = |\overline{AB}| = R_s - g_0\delta_s\cos\alpha_m \pm \sqrt{\left(g_0\delta_s\cos\alpha_m\right)^2 - g_0^2\delta_s^2 + R_r^2}. \tag{12}$$

Since $R_r \gg g_0\delta_s$, and the air-gap length should be smaller than R_s, (12) can be further simplified as

$$g(\alpha_m) \approx R_s - g_0\delta_s\cos\alpha_m - R_r = g_0 - g_0\delta_s\cos\alpha_m$$
$$= g_0\left(1 - \delta_s\cos\alpha_m\right). \tag{13}$$

Finally, PPUA in normal condition and SAGE case can be expressed as
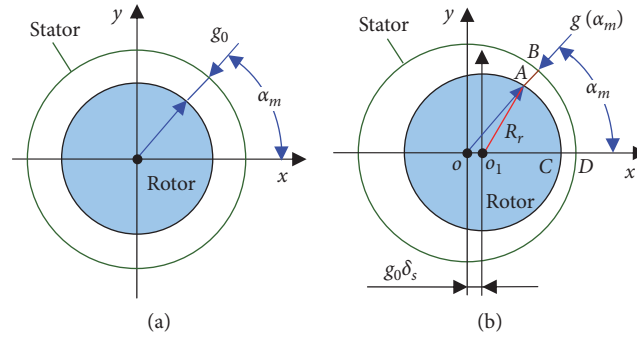
FIGURE 2: Air gap of generator: (a) normal; (b) radial SAGE.

$$\begin{cases} \Lambda(\alpha_m, t) = \dfrac{\mu_0}{g_0} = \Lambda_0 \cdots\cdots\cdots\cdots\cdots\cdots\cdots\cdots\cdots\cdots\cdots\cdots\cdots\cdots\cdots\cdots\cdots\cdots\cdots\cdots\cdots\cdots\cdots \text{Normal,} \\[12pt] \Lambda(\alpha_m, t) = \dfrac{\mu_0}{g(\alpha_m, t)} = \dfrac{\mu_0}{g_0(1 - \delta_s \cos \alpha_m)} = \Lambda_0\left(1 + \delta_s \cos \alpha_m + \delta_s^2 \cos^2 \alpha_m + \cdots\right) \\[12pt] \approx \Lambda_0\left(1 + \delta_s \cos \alpha_m + 0.5\delta_s^2 + 0.5\delta_s^2 \cos 2\alpha_m\right)\cdots\cdots\cdots\cdots\cdots \text{SAGE,} \end{cases} \quad (14)$$

where the second equation is expanded by power series.

2.3. Impact of SISC and SAGE on MMF. When the combined fault occurs, i.e., when SISC and SAGE take place at the same time, both MMF and PPUA will be changed. Simply multiplying equation (7) by (14), the final MFD can be obtained. However, another factor, namely, the short circuit position, will actually impact on the final MFD as well. This can be explained by Figures 1 and 3(a). When there is no SAGE, i.e., in the ideally normal condition, the short circuit position should have no impact on the MMF/MFD due to the symmetric distribution of the armature windings. However, as long as SAGE exists, the short circuit position will act on the amplitude of the short circuit current. When the short circuit turns (indicated by the central axis position of the turns) are closer to the minimum air gap (see Figure 3(a), $\alpha_m = 0$), the induced short circuit current I_s (see Figure 1) will be larger since the PPUA has a larger value (see equation (14)).

By considering the short circuit position, equation (2) modifies to

$$f_d(\alpha_m, t) = F_d\left(\frac{1 - \delta_s}{1 - \delta_s \cos \alpha_{sm}}\right) \cos \omega t \cos(\alpha_m - \alpha_{sm})$$

$$= \rho F_{d+} \cos(\omega t + \alpha_m - \alpha_{sm}) + \rho F_{d-} \cos(\omega t - \alpha_m + \alpha_{sm}), \quad (15)$$

where $\rho = (1 - \delta_s)/(1 - \delta_s \cos \alpha_{sm})$ which is a coefficient of the MMF at the short circuit position to the MMF at the minimum air-gap point. Obviously, this coefficient depends on SISC position (see Figures 1 and 3(a)). For more clarity, the relation of ρ vs. α_{sm} is illustrated in Figure 3(b).

As indicated in Figure 3(b), the developing regularity of ρ changes similarly to the cosine function. When

$a_{sm} = 0$, ρ will obtain its max value. This means when the short circuit takes place in the winding whose central line coincides with the minimum air-gap point, SISC will have the maximum impact on MFD/MMF, i.e., MFD/MMF will be decreased most. Moreover, the more severe the SAGE degree is, the larger the amplitude variation of ρ will be. In general, the effect of the closer short circuit position to the minimum air-gap point on MFD is similar to the more severe SISC degree; this conclusion has been also obtained in [22]. Although a generator may have the SAGE degree to different extent, such law still exists even when the SAGE degree is 2% or smaller. Consequently, the final MMF in the air gap for the combined fault is modified to

$$f(\alpha_m, t) = F_{r1+}\cos\left(\omega t - p\alpha_m + \psi + \frac{\pi}{2}\right) + F_{s1+}\cos(\omega t - p\alpha_m)$$

$$+ \rho F_{r1-}\cos\left(\omega t + p\alpha_m - \psi - \frac{\pi}{2}\right) + \rho F_{s1-}\cos(\omega t + p\alpha_m)$$

$$+ \rho F_{r3+}\cos\left(3\omega t - p\alpha_m + \psi + \frac{\pi}{2}\right) + \rho F_{s3+}\cos(3\omega t - p\alpha_m). \quad (16)$$

Since the impact of the closer short circuit position to the minimum air-gap point can be similarly treated as a severe SISC degree, for the sake of concision, in this paper, we mainly focus on the influence of the fault types and fault degrees on the EMT ripples, while the variation difference due to varied SISC position will not be fully expanded.

2.4. EMTs in Different Running Conditions. In this paper, we employ the principle of virtual power to derivate the EMT expression. The air-gap magnetic energy can be calculated via [20]

(a)

(b)
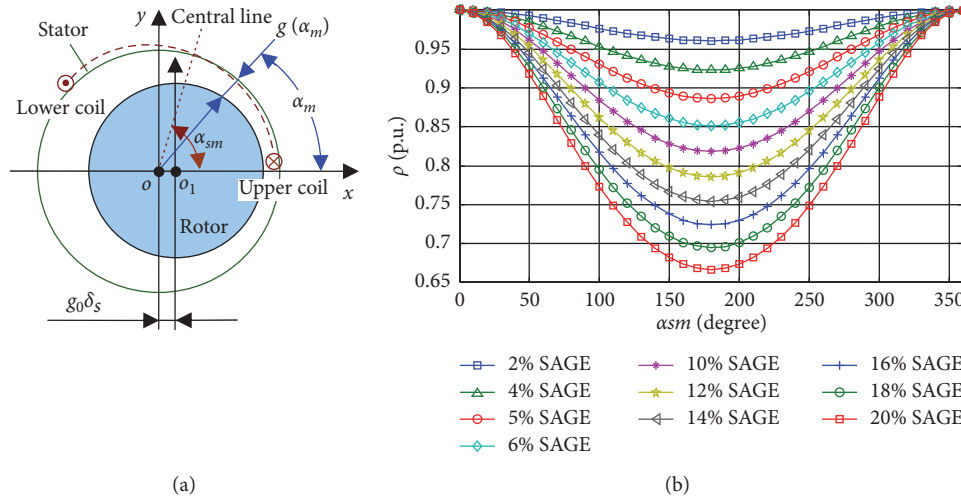
FIGURE 3: Impact of short circuit position on PPUA: (a) diagram to show the short circuit position; (b) relation of ρ vs. α_{sm}.

$$W = \frac{1}{2}L\int_0^{2\pi}\left\{R(\alpha_m,t)\Lambda(\alpha_m,t)[f(\alpha_m,t)]^2\right\}d\alpha_m, \quad (17)$$

where L is the axial length of the stator core and $R(\alpha_m, t)$ is the average radius of the air gap which can be written as

$$R(\alpha_m,t) = \begin{cases} R_0 \cdots\cdots\cdots\cdots\cdots \text{(Normal \& SISC)} \\ \\ R_0 - \dfrac{g_0\delta_s\cos\alpha_m}{2}\cdots\cdots \text{(SAGE \& CF)} \end{cases} \quad (18)$$

According to the principle of virtual displacement (see Figure 4), if the rotor MMF has a differential displacement $\Delta\psi$, then a resistant EMT will be generated which can be written as [6]

$$T = p\frac{\partial W}{\partial\psi}. \quad (19)$$

According to the MMF and PPUA derived previously (see (7), (14), and (16)), the EMTs in normal condition, SAGE fault, SISC fault, and the CF cases can be written as

$$\begin{cases} T_{\text{Normal}} = -\Pi I_{f0}^2\lambda\cos\psi, \\[2mm] T_{\text{SAGE}} = -\dfrac{1}{2}\Pi I_{f0}^2\left\{e\left[\lambda\cos(2\omega t+\psi)+\cos\left(2\omega t+2\psi+\dfrac{\pi}{2}\right)\right]+2\lambda(e+1)\cos\psi\right\}, \\[2mm] T_{\text{SISC}} = -\Pi I_{f0}^2\lambda\{2v^2\cos\psi+2v[\cos(2\omega t+\psi)+\cos(2\omega t-\psi)]+v^2[\cos(4\omega t+\psi)+\cos(4\omega t-\psi)]\}, \\[2mm] T_{\text{CF}} = -\dfrac{1}{2}\Pi\left\{\begin{array}{l} I_{f0}^2\lambda[4(1+e)v\rho+2e\rho^2v^2]\cos(2\omega t+\psi)+I_{f0}^2\lambda[4(1+e)v\rho+\rho^2v^2]\cos(-2\omega t+\psi) \\[2mm] +e(I_{f0}^2+\rho^2vI_{f2}I_{f0})\cos(2\omega t+2\psi+0.5\pi)+0.5e\rho^2vI_{f2}I_{f0}\cos(-2\omega t+2\psi+0.5\pi) \\[2mm] +2I_{f0}^2\lambda[(1+e)v^2\rho^2+e\rho v]\cos(4\omega t+\psi)+2(1+e)I_{f0}^2\lambda v^2\rho^2\cos(-4\omega t+\psi) \\[2mm] +e\rho I_{f2}I_{f0}\cos(4\omega t+2\psi+0.5\pi)+eI_{f0}^2\lambda\rho^2v^2\cos(6\omega t+\psi)+e\lambda\rho I_{f2}I_{f0}\cos(2\psi+0.5\pi) \\[2mm] +0.5e\rho^2vI_{f2}I_{f0}\cos(6\omega t+2\psi+0.5\pi)+\left[2(1+e)I_{f0}^2\lambda(2v^2\rho^2)+2e\rho v\right]\cos\psi \end{array}\right\}, \end{cases} \quad (20)$$
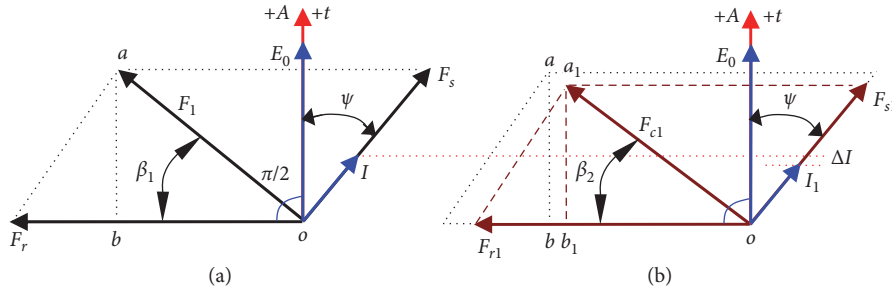
where

Figure 4: Diagram of MMF vectors. (a) Normal. (b) SISC.

$$\begin{cases} \Pi = p\Lambda_0 N^2 L R_0 \pi, \\ \\ \lambda = \dfrac{F_{s1+}}{F_{r1+}} = \dfrac{F_s}{F_r}, \\ \\ e = \left(\dfrac{1}{2} - \dfrac{g_0}{4R_0}\right)\delta_s^2, \\ \\ \nu = \dfrac{F_{s3+}}{F_{s1+}} = \dfrac{F_{r3+}}{F_{r1+}}, \end{cases} \tag{21}$$

where e and ν represent the degrees of SAGE and SISC, respectively. The greater their values are, the more serious the fault will be. As indicated in (20), there is only a DC component in normal condition. However, the occurrence of SAGE will bring in extra 2nd harmonic to EMT, while SISC will primarily induce the 2nd and 4th harmonics. For the combined faults, an extra 6th harmonic will be newly produced in addition to the 2nd and 4th ones induced by the two single faults. Significantly, this ripple component difference can be employed to identify and diagnose the fault types. To be more distinct, the upper amplitude formulas, the influential factors, and the developing tendencies are listed in Table 1.

3. FEA and Experiment Validation

3.1. FEA and Experiment Setup. In this paper, the CS-5 prototype generator, which was designed and manufactured ourselves, is used for the 2D finite element calculation and the experimental test. The main parameters are shown in Table 2.

The generator rotor is kept stable by the bearing blocks, while the stator can be moved along both the radial and the axial directions. The movements are controlled by four dial indicators and confirmed by the high-precision filler gauges (see Figures 5(a) and 5(b)). Two indicators are for the radial movement while the other two are for the axial movement. On the generator, there is a plate with several short circuit taps in phases A and B (see Figures 5(c) and 5(d)). By setting varied SAGE values and connecting different short circuit taps, different running conditions including single and combined faults can be simulated.

The established finite element model is illustrated in Figures 5(e) and 5(f). During FEA, the rotor core as well as

the field windings is shifted along X axis (to the right) to simulate SAGE (see Figure 5(e)). The SISC fault is simulated by both the external coupling circuit (the switch S-A1 in Figure 5(e)) and the physical model (the failure windings are divided into two parts: one is to simulate the healthy windings while the other is to simulate the short circuit part (see Figure 5(g)). By adjusting the turn numbers of LA1 (short circuit part) and LPhaseA1 (the healthy part) indicated in Figure 5(g), different SISC fault degrees can be simulated.

During the FEA calculation, the parameters are set to the same as the experiments. Four groups of experiments and FEA calculations as follows are carried out, respectively.

(1) Normal condition: there is neither SAGE nor SISC. EMT values are collected as reference.

(2) SAGE cases: 10%, 20%, and 30% SAGE conditions are set, respectively.

(3) SISC cases: 3%, 6%, and 9% SISC conditions are taken, respectively.

(4) CF cases: (1) combined faults of stable SAGE and varied SISC degrees, including 10% SAGE and 3%, 6%, and 9% SISC, 20% SAGE and 3%, 6%, and 9% SISC, and 30% SAGE and 3%, 6%, and 9% SISC and (2) combined faults of stable SISC and varied SAGE degrees, including 3% SISC and 10%, 20%, and 30% SAGE, 6% SISC and 10%, 20%, and 30% SAGE, and 9% SISC and 10%, 20%, and 30% SAGE are taken, respectively.

During the experiment, the electromagnetic torque can be usually measured in two means in general. One is the direct means which is primarily based on the torquemeter, and the other is the indirect means primarily based on the equivalent energy conversion calculation. In this paper, we employ the indirect means. The key thought is that the energy of the electromagnetic torque should be equivalent to the output power when the generator is under a steady running state, no matter healthy or faulty. The electromagnetic torque energy conversion model is illustrated in Figure 5(f), where the power of the rotor is $F_t^* R\Delta\theta = T^*\omega$, and it should be equivalent to the power of the stator $(U_A I_A + U_B I_B + U_C I_C)\cos\varphi$. Then, the EMT is calculated via

$$T = \frac{P}{\omega} = \frac{(U_A I_A + U_B I_B + U_C I_C)\cos\varphi}{2\pi n/60}, \tag{22}$$

TABLE 1: EMT upper amplitude formulas and influential factors.

Harmonic	Case	Amplitude formulas $(x0.5\prod[I_{f0}])$	Factors	Trend
2nd	Normal	—	—	↑
	SAGE	$I_{f0}e\sqrt{\lambda^2+1+2\lambda\cos(\psi+0.5\pi)}$	I_{f0}, δ_s	↑
	SISC	$4I_{f0}\lambda v\sqrt{2+\cos 2\psi}$	I_{f0}, I_{f2}	
	CF	$\sqrt{\begin{aligned}&I_{f0}^2\lambda\{8(1+e)vp(1+\cos 2\psi)[4vp+e(\rho^2v^2+\rho v^2+1)]+\rho^4v^4+e(\rho^2v^2+\rho v^2+1)\times[\rho^2v^2(e+2\cos 2\psi)+e(\rho v^2+1)]\}\\&+e^2\{\rho^2vI_{f2}(I_{f0}+\rho^2vI_{f2})[2+\cos(4\psi+\pi)]-0.75\rho^4v^2I_{f2}^2+I_{f0}^2\}\\&+2I_{f0}^2\lambda e(I_{f0}+\rho^2vI_{f2})\{[4(1+e)vp+e(\rho^2v^2+\rho v^2+1)]\times\cos(\psi+0.5\pi)+[4(1+e)vp+\rho^2v^2]\cos(\psi+0.5\pi)\}\\&+I_{f0}^3I_{f2}e\lambda\rho^2[4(1+e)vp+e(\rho^2v^2+\rho v^2+1)]\cos(\psi+0.5\pi)+4(1+e)vp+\rho^2v^2\}\end{aligned}}$	I_{f0}, δ_s, I_{f2}	↑

Harmonic	Case	*Amplitude formulas* $(x0.5\prod[If0])$	*Factors*	*Trend*
4th	Normal	—	—	—
	SAGE	—	—	↑
	SISC	$2I_{f0}\lambda v^2\sqrt{2+\cos 2\psi}$	I_{f0}, I_{f2}	↑
	CF	$2\rho\sqrt{\begin{aligned}&I_{f0}^2\lambda^2\{2vp(1+e)(1+\cos 2\psi)[(1+e)vp+1]+e^2\}\\&+evI_{f0}I_{f2}[[(1+e)vp+e]\cos(\psi+0.5\pi)+(1+e)vp\cos(3\psi+0.5\pi)]+0.25e^2I_{f2}^2\end{aligned}}$	I_{f0}, δ_s, I_{f2}	
6th	Normal	—	—	—
	SAGE	—	—	—
	SISC	—	—	↑
	CF	$evp^2\sqrt{\lambda^2v^2I_{f0}^2+0.25I_{f2}^2+\lambda vI_{f0}I_{f2}\cos(\psi+0.5\pi)}$	I_{f0}, δ_s, I_{f2}	

TABLE 2: Key parameters of CS-5 prototype generator.

Parameters	Values	Parameters	Values
Poles	2	Rated rotating speed	3000 rpm
Rated power	5 kVA	Stator core length	130 mm
Pole pairs	1	Stator winding turns per slot	22
Rated power factor ($\cos\varphi$)	0.8	Rotor slots	16
Radius of air-gap	1.2 mm	Outer diameter of rotor core	142.6 mm
Stator slots	36	Inner diameter of rotor core	40 mm
Outer diameter of stator core	250.5 mm	Rotor winding turns per slot	60
Inner diameter of stator core	145 mm	Internal power factor ($\cos\psi$)	0.62
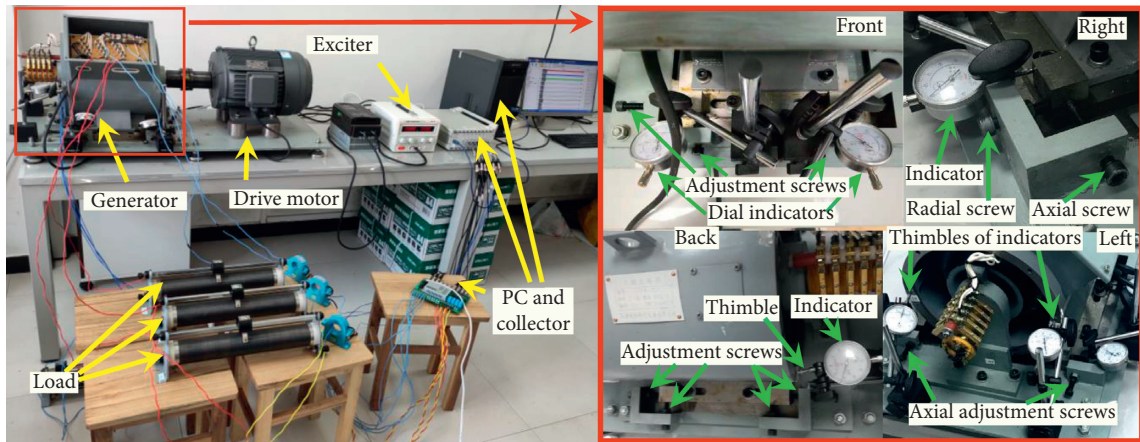
(a)

(b)
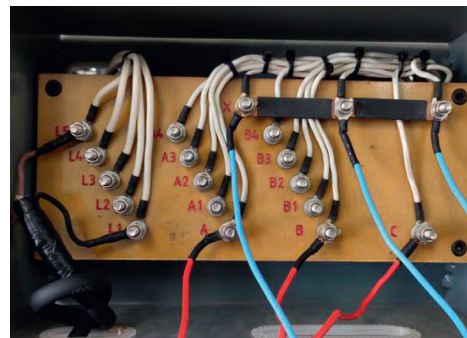
(c)
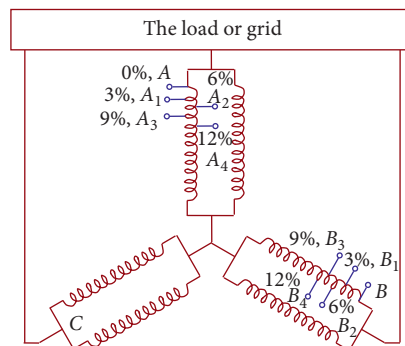
(d)

FIGURE 5: Continued.
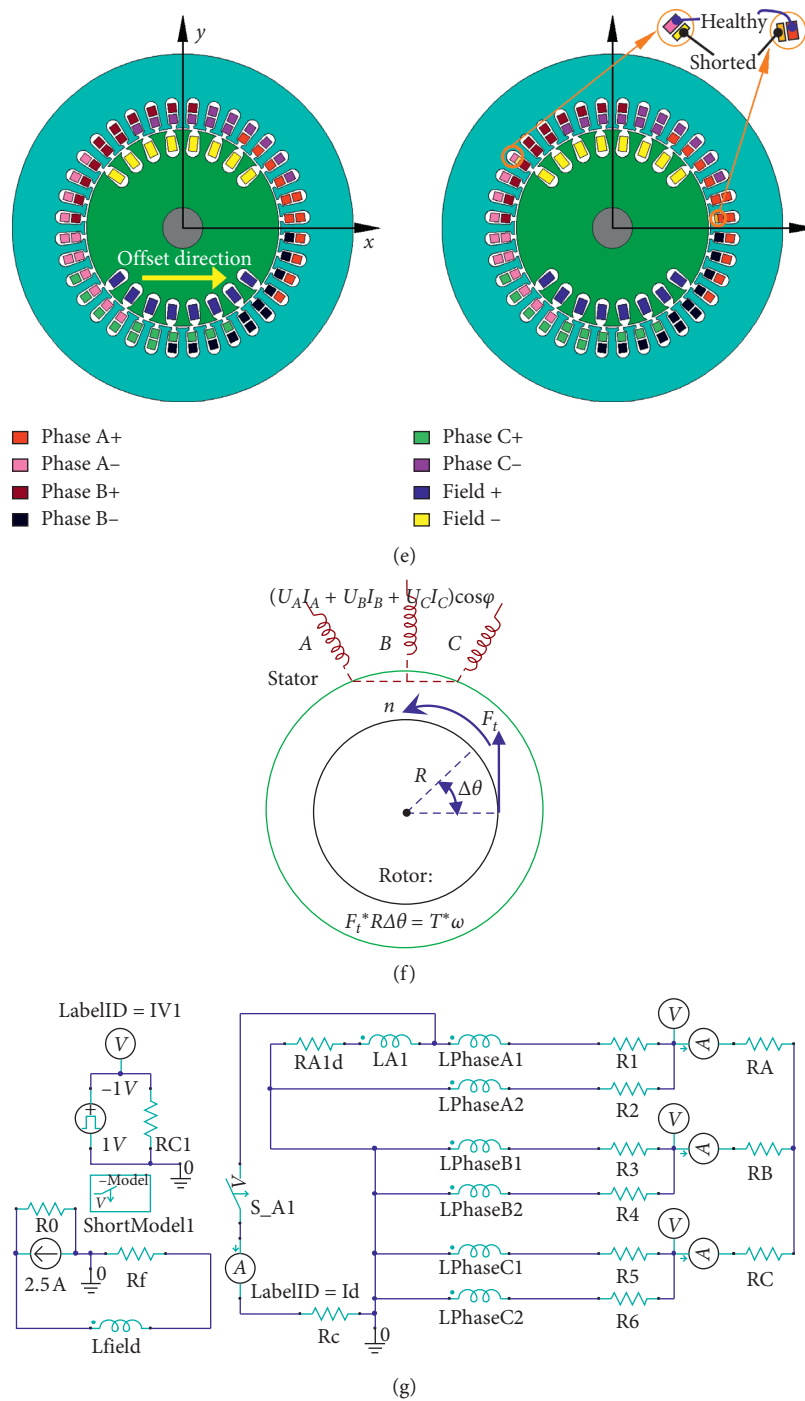
FIGURE 5: CS-5 prototype generator: (a) picture of the generator set, (b) high-precision gauges, (c) picture of short circuit taps, (d) short circuit tap set, (e) physical 2D model, (f) electromagnetic torque energy conversion model, and (g) coupling circuit model.

where U_A, U_B, and U_C are the three-phase voltages, I_A, I_B, and I_C are the three-phase currents, n is the rotating speed of the rotor, and $\cos\varphi$ is the power factor.

3.2. Results and Discussion for SAGE Faults. The EMTs before and after SAGE by FEA are illustrated in Figure 6, while the results by experiment are indicated in Figure 7. It is shown that the occurrence of SAGE will increase the general EMT.

The severer the SAGE degree is, the more the EMT increment will be.. For the spectrum components, both the FEA result and the experimental data show that the 2nd harmonic is the prominent one whose amplitude will be greatly intensified by SAGE. Although the amplitude values of the FEA and the experimental results are not exactly equal, their developing tendencies are generally consistent with each other. Also, both the FEA results and the experiment data follow the previously theoretical analysis conclusion (see equation (20)).
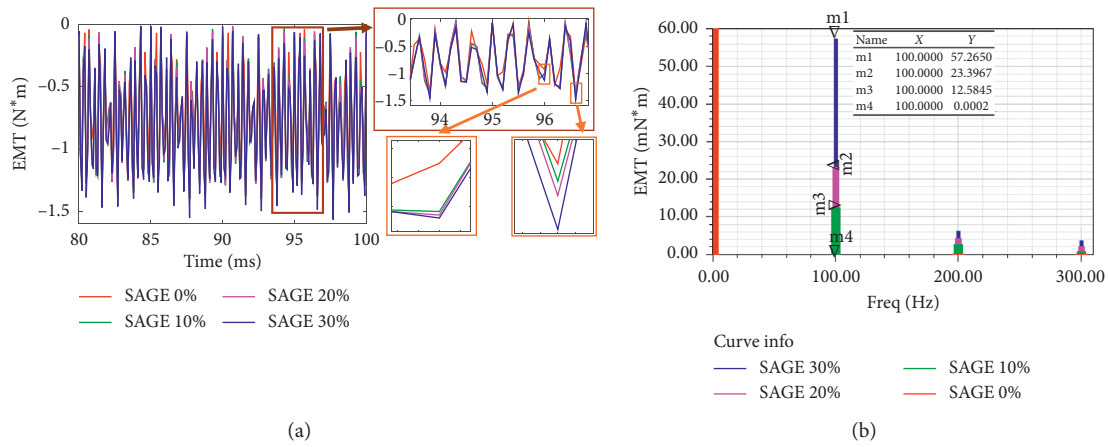
FIGURE 6: EMT before and after SAGE by FEA: (a) time-domain waveforms and (b) EMT spectra.
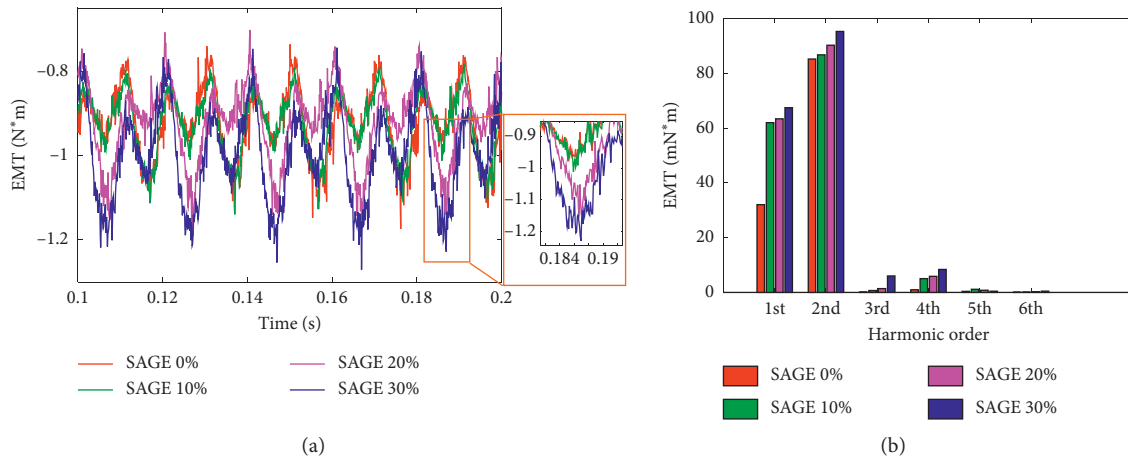
FIGURE 7: EMT before and after SAGE by experiment: (a) time-domain waveforms and (b) spectra.

Actually, in addition to the 2nd harmonic, there are still 4th and 6th harmonics showing the increasing tendency. The reason for this is the presence of higher-order MMF harmonics. In Figure 2 and equation (20), only the 1st harmonic MMF is taken into account, while other higher-order harmonics are ignored. If we consider the higher-order harmonics such as the 3rd and 5th, the square of the MMF (see equation (17)) will lead to the appearance of the even EMT harmonics including 2nd, 4th, 6th, etc. Since the fundamental-frequency MMF component has the largest amplitude, the 2nd EMT harmonic which is mainly the square of the 1st MMF will be the most prominent one.

It is also suggested from Figures 6 and 7 that the occurrence of SAGE will generally increase the DC value of EMT (the curves are shifting upward to the larger value direction). This result well follows equation (14). According to (14), for the SAGE case, there is an extra factor $0.5\delta_s^2$ which will of course increase the DC value (see equation (17)) as the occurrence and increment of SAGE.

Theoretically, there should be only even harmonics in both normal and SAGE cases since the MMF has only odd harmonics (the square operation in equation (17) will produce only even harmonics). However, the experimental result indicated in Figure 7 appears to be odd harmonic. This is primarily caused by two factors. On the one hand, the exciting current is transferred by the rectifier from the AC current and actually includes residual harmonics. In other words, the exciting current is not an ideal DC current. On the other hand, the actual rotor surface is not a strict circle. The slots and the uneven roundness inform a dynamic eccentricity which will produce odd harmonics in EMT (there will be an extra ωt factor in the permeance expression in equations (14) and (17)).

The FEA and the experimental results are compared in Figure 8. It is shown that although the test EMT amplitude increment cannot exactly match the FEA dada, the general developing tendencies are still in accordance. To confirm the data differences, we have redone the experiments and carried out the FEA calculation three times, but the data gap shows the same result. The probable reason may be related to both the manufacturing level and the calculation error.

3.3. Results and Discussion for SISC Faults. The time-domain waves as well as the spectra by FEA and experiment are
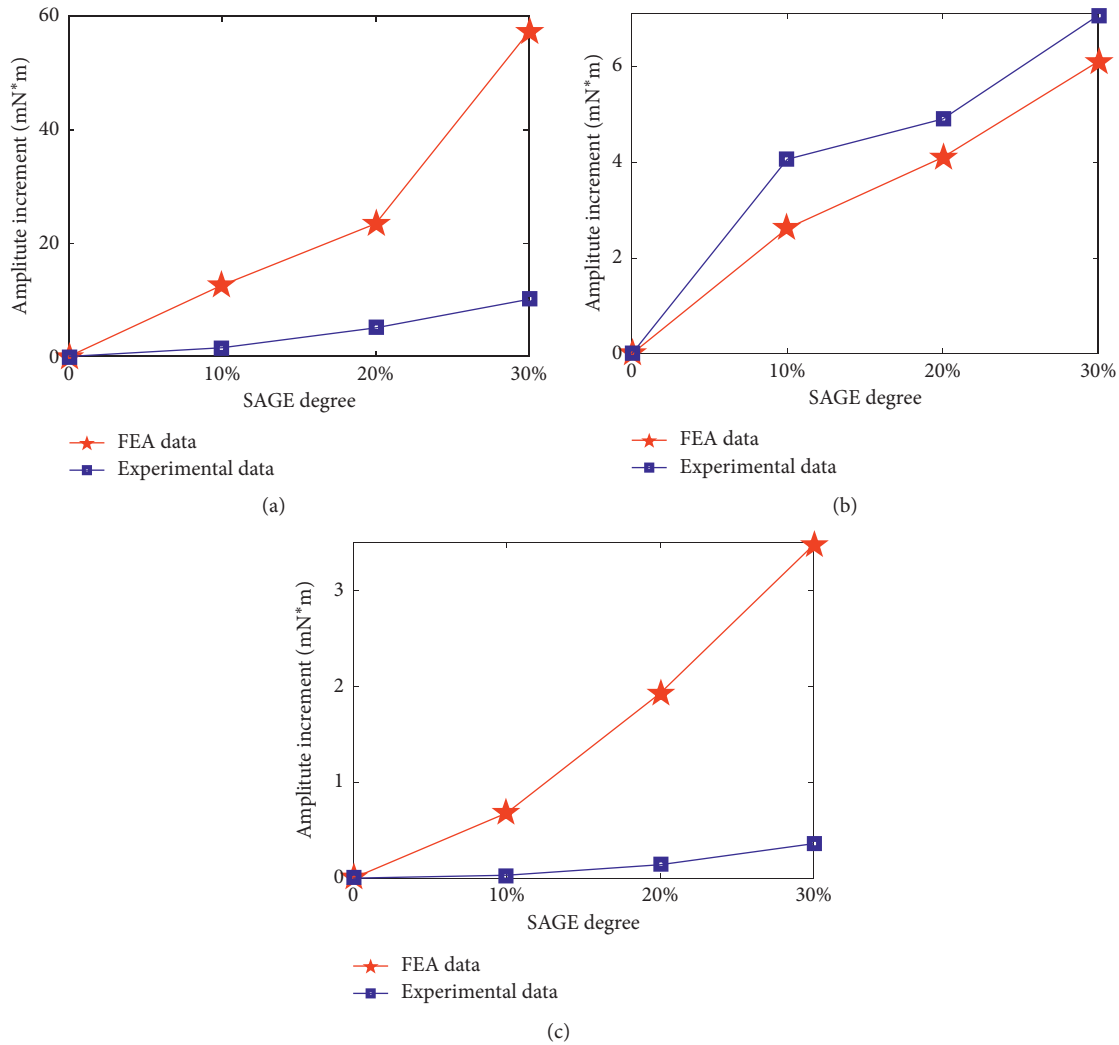
FIGURE 8: FEA and experiment comparison in SAGE cases: (a) 2nd harmonic, (b) 4th harmonic, and (c) 6th harmonic.

illustrated in Figures 9 and 10, respectively. It is shown that the EMT ripples, especially the 2nd and the 4th harmonics, will be increased as SISC takes place. The more severe the SISC is, the larger the harmonic amplitudes will be.

As indicated in Figure 10, there are still odd harmonics in the experiment result. The very reason is just the same as previously mentioned in Section 3.2. In general, the FEA results are in accordance with the experiment data. Also, both the FEA and the experimental results are consistent with the theoretical analysis conclusion drawn from equation (20) and Table 1.

The result comparison between the FEA result and the test data is illustrated in Figure 11. Similar to SAGE case, the EMT amplitude increment by FEA and experiment still has a data gap, while the overall developing tendencies of the two data types still match with each other.

3.4. Results and Discussion for Combined Faults. The detailed EMT results under combined faults are illustrated in Figures 12–15. To be more comprehensive, two groups of combined faults are simulated by both FEA and experiment. One is to keep the SAGE degree as stable while changing the SISC degrees, and the other is to keep the SISC degree as stable while changing the SAGE degrees. More details about the fault simulation can be sound in.

As indicated in Figure 12, in the combined fault cases, the increment of SAGE will increase the 2nd, 4th, and 6th EMT harmonics. Moreover, comparing Figures 12(a)–12(c) with Figure 9(b), it shows that the harmonic amplitude increment under the combined fault is larger than that under the single SISC fault. On the contrary, the comparison between Figures 12(d)–12(f) and 6(b) suggests that the EMT harmonic increment in the combined fault cases is smaller than that of the single SAGE fault. The comparison result in the experimental data shows the similar result (see Figures 13, 10, and 7). The experimental results indicated in Figure 13 generally follow the developing tendencies obtained by FEA. The primary difference between the experimental and the FEA results is that there are odd harmonics, especially the 1st harmonic, existing in the spectra. The very reason, which has been mentioned previously, is that there is
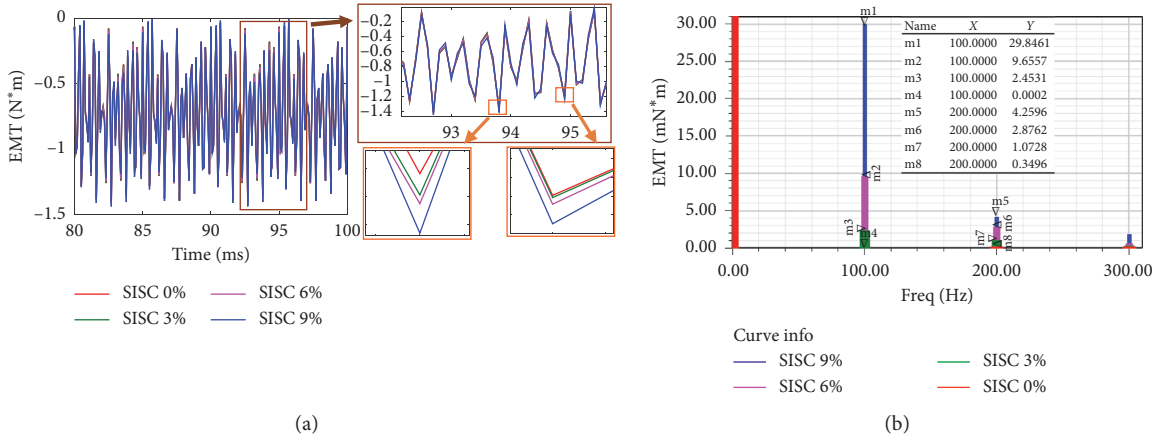
FIGURE 9: EMT under SISC fault. (a) Time-domain waveform. (b) Spectrum of EMT in different SISC degrees.
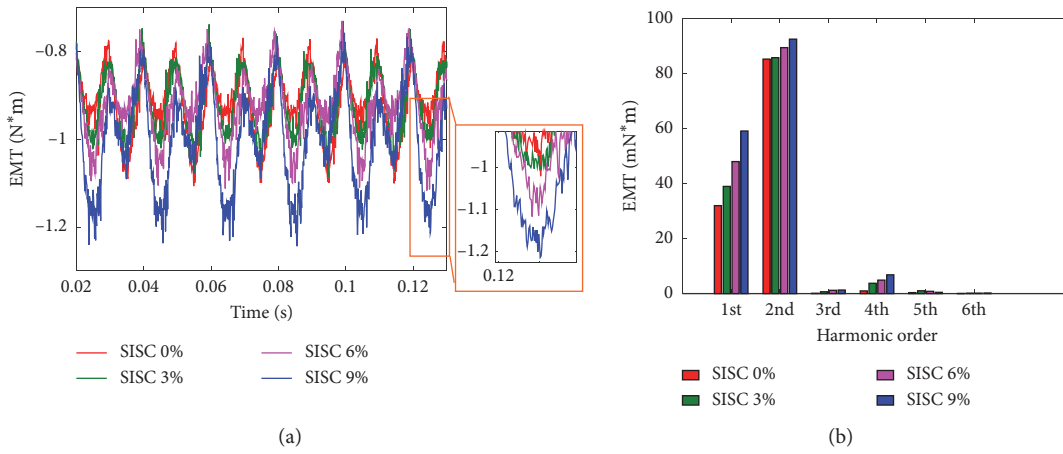
FIGURE 10: Experimental data of EMT under different SISC degrees: (a) time-domain waveform and (b) spectrum.

somewhat dynamic eccentricity due to the slots and the uneven roundness of the rotor, and the exciting current transferred by the rectifier is not standard DC current.

Comparing Figure 13 with Figure 12, it is shown that the ripple amplitudes by the experiment are smaller than those obtained by FEA. The reason for this mainly lies in the constraint difference between the FEA calculation and the experiment. During FEA, it is assumed under an ideal condition. For instance, the energy conversion is treated as no extra loss, while actually part of the energy will be consumed due to different kinds of losses. This means, the sum of the actual EMT energy and the loss energy equals to the input mechanical torque energy, while in FEA, the mechanical torque energy is generally treated as equivalent to the EMT energy. Therefore, the actual EMT as well as the ripples should be smaller than the FEA results.

More details about the difference between the FEA result and the experimental data are illustrated in Figures 14 and 15. Although there is still data gap between the FEA and the experimental results, the developing tendencies match well. Comparing Figure 14 with Figure 15, it is suggested that the gradients of the curves in Figure 15 (for the SISC increased

cases) are larger than those in Figure 14. This means in the combined fault cases, SISC has a more intensive impact on the EMT ripple amplitude increment.

3.5. Comparison between Single and Combined Faults. To compare the impact of the single and the combined faults on the EMT ripple properties in detail, we collect all the component amplitude increment data for the further analysis (see Figures 16–18).

As indicated in Figure 16, the gradients of the SISC curves are larger than those of the SAGE cases (the polylines for the SISC faults are sharper). This means the impact sensitivity of the single SISC fault is more intensive than that of the SAGE fault. Although the fault degrees for these two single faults are different, the sensitivity index is calculated with the same formula which can be written as

$$S = \frac{\Delta T}{\Delta F_d}, \tag{23}$$

where ΔT is the variation of EMT and ΔF_d is the variation of the fault degree.
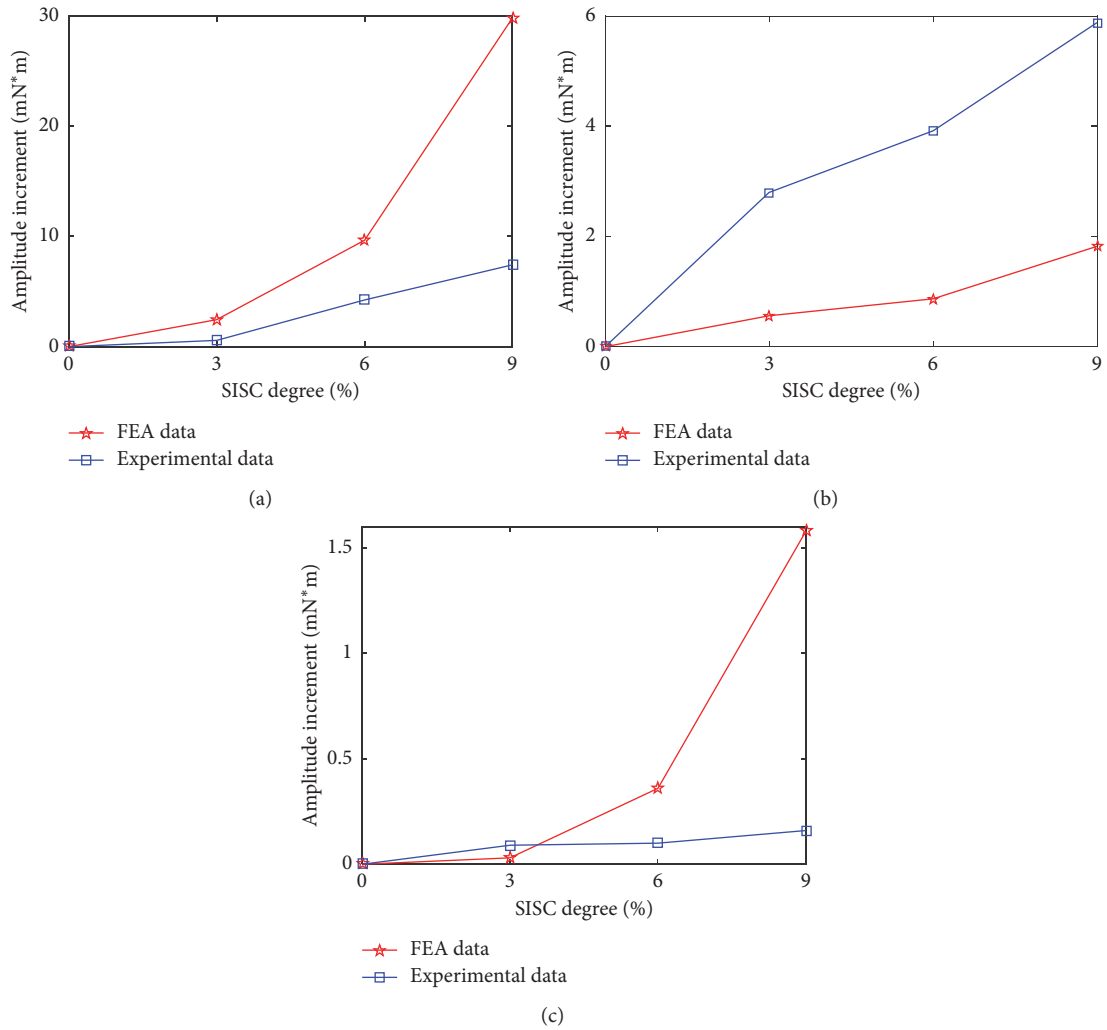
FIGURE 11: FEA and experiment comparison in SISC cases: (a) 2nd harmonic, (b) 4th harmonic, and (c) 6th harmonic.
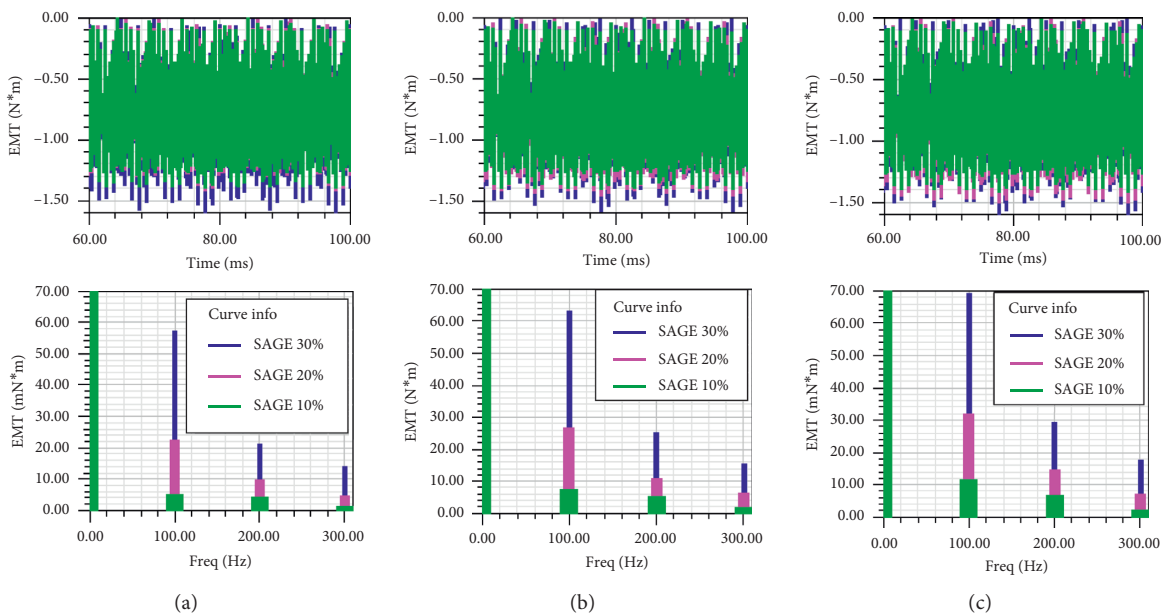
FIGURE 12: Continued.

(d)

(e)

(f)
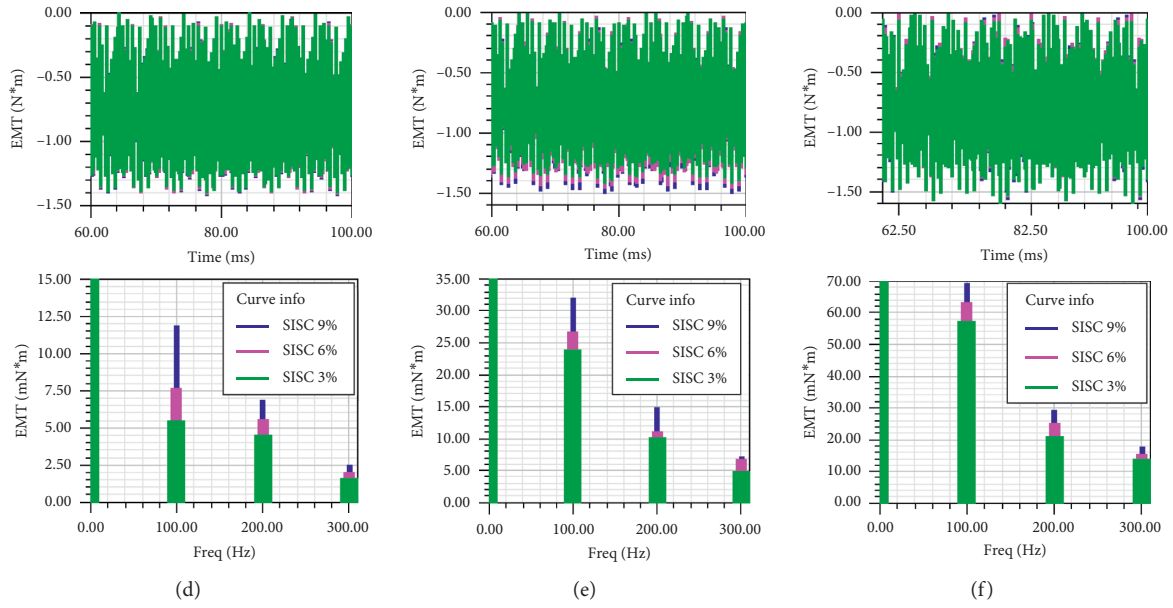
FIGURE 12: EMT curves and spectra in CF cases by FEA: (a) SISC 3% and different SAGE degrees, (b) SISC 6% and different SAGE degrees, (c) SISC 3% and different SAGE degrees, (d) SAGE 10% and different SISC degrees, (e) SAGE 20% and different SISC degrees, and (f) SAGE 30% and different SISC degrees.

(a)

(b)

(c)
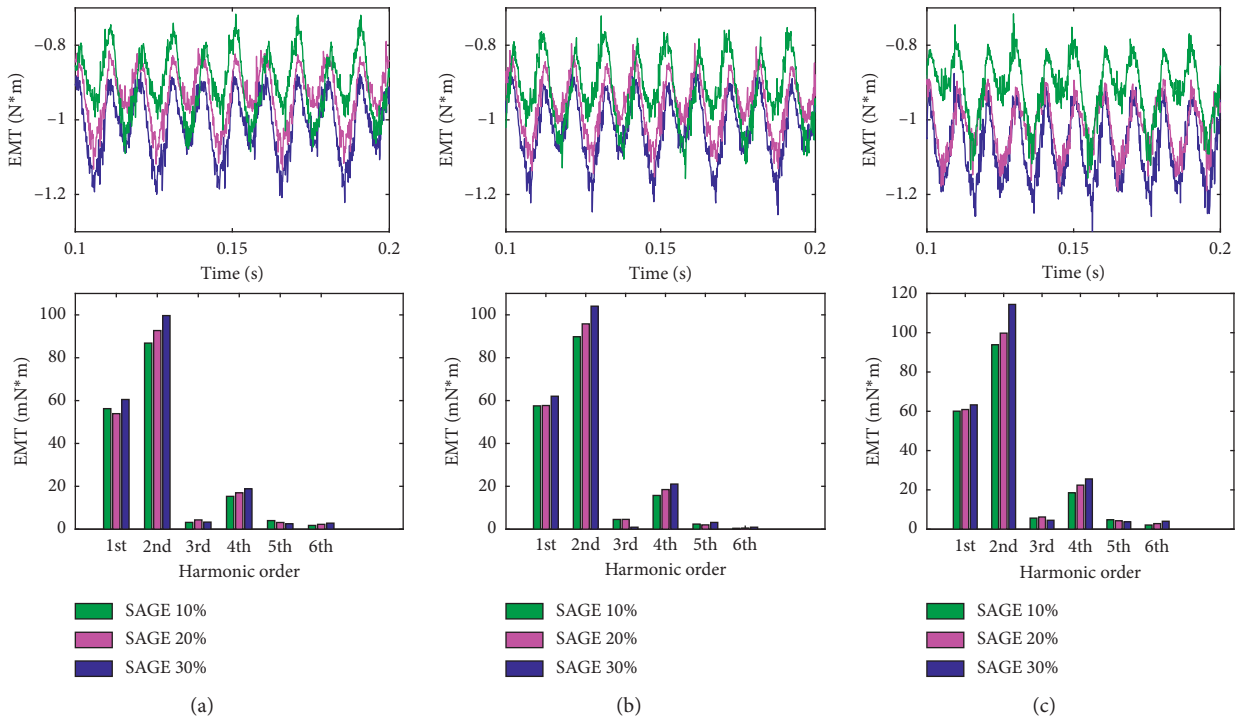
FIGURE 13: Continued.
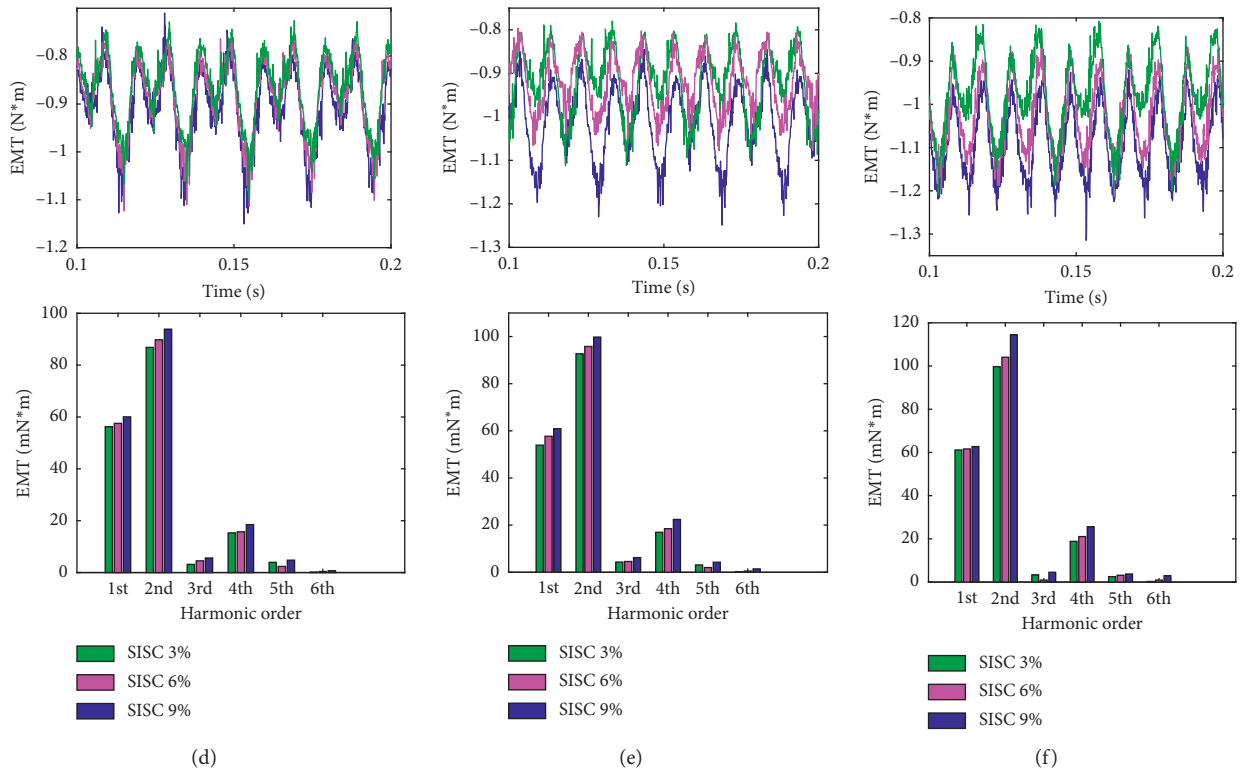
FIGURE 13: EMT curves and spectra in CF cases by experiment: (a) SISC 3% and different SAGE degrees, (b) SISC 6% and different SAGE degrees, (c) SISC 3% and different SAGE degrees, (d) SAGE 10% and different SISC degrees, (e) SAGE 20% and different SISC degrees, and (f) SAGE 30% and different SISC degrees.
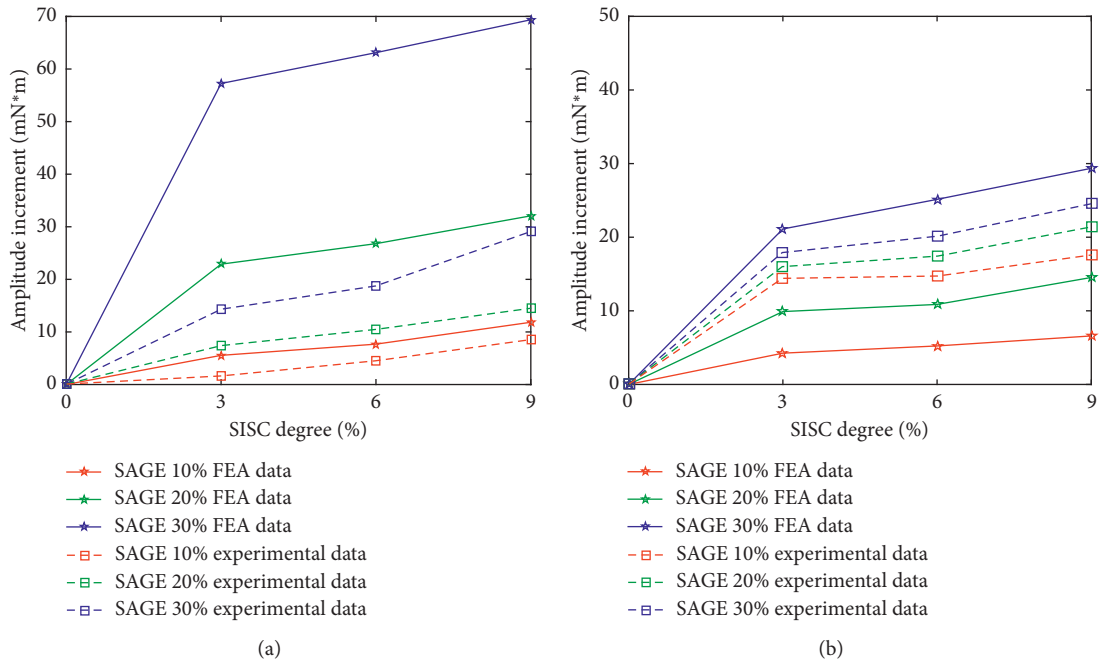
FIGURE 14: Continued.
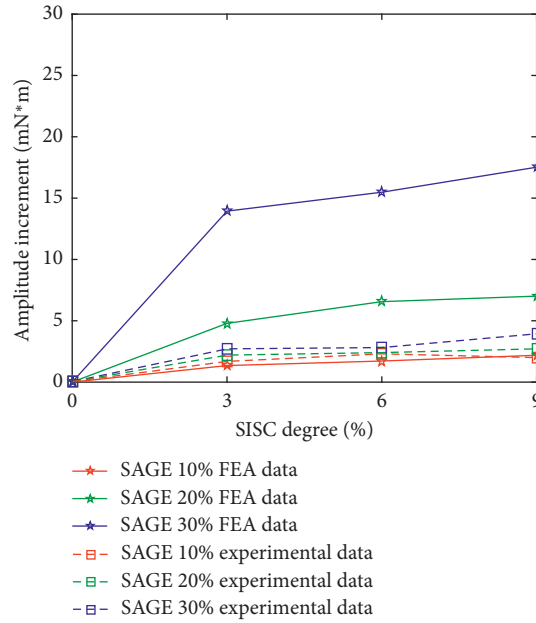
(c)

FIGURE 14: FEA and experiment comparison in CF cases with increased SAGE: (a) 2nd harmonic, (b) 4th harmonic, and (c) 6th harmonic.
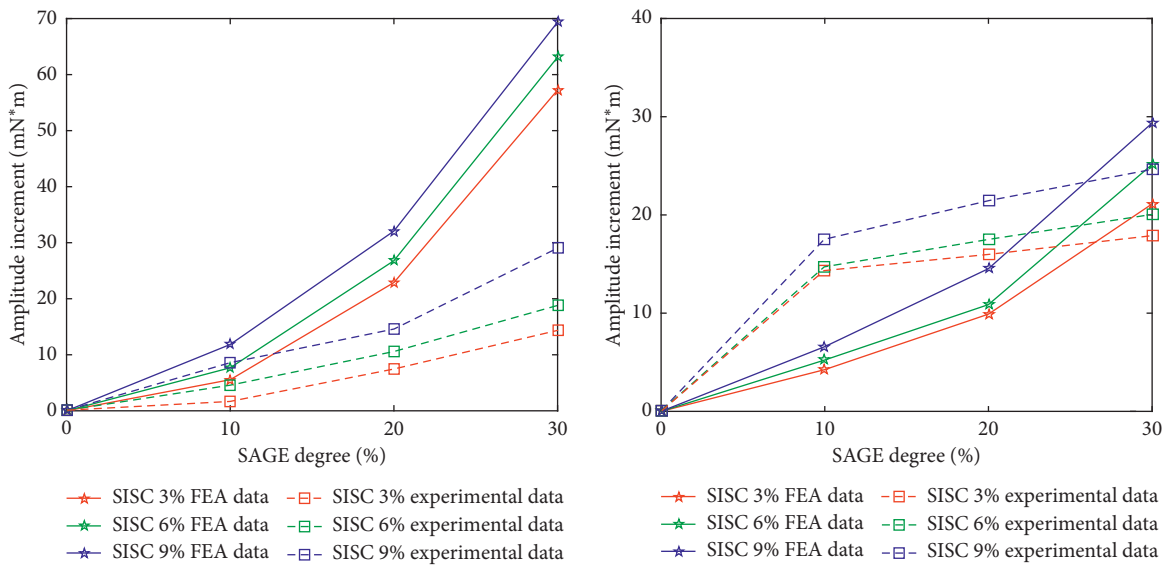
(a)

(b)

FIGURE 15: Continued.

(c)
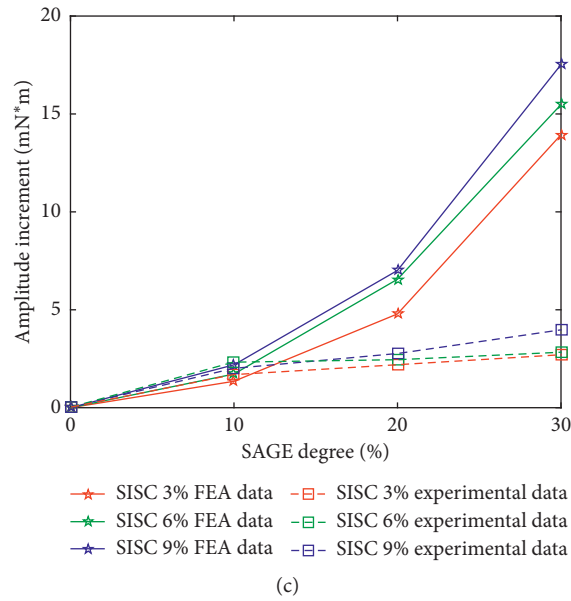
FIGURE 15: FEA and experiment comparison in CF cases with increased SISC: (a) 2nd harmonic, (b) 4th harmonic, and (c) 6th harmonic.

(a)

(b)

(c)
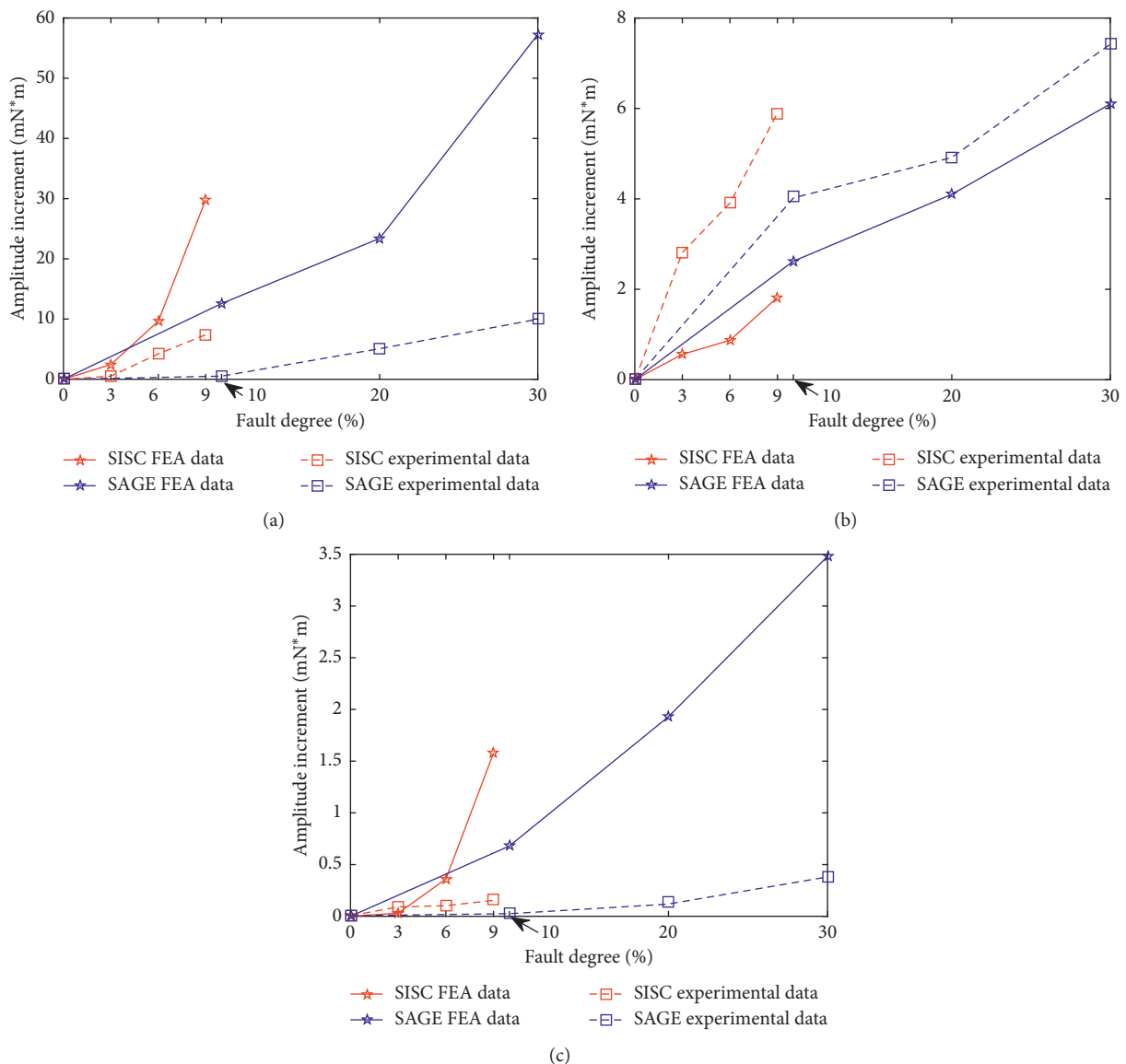
FIGURE 16: Impact comparison for single faults: (a) 2nd harmonic, (b) 4th harmonic, and (c) 6th harmonic.
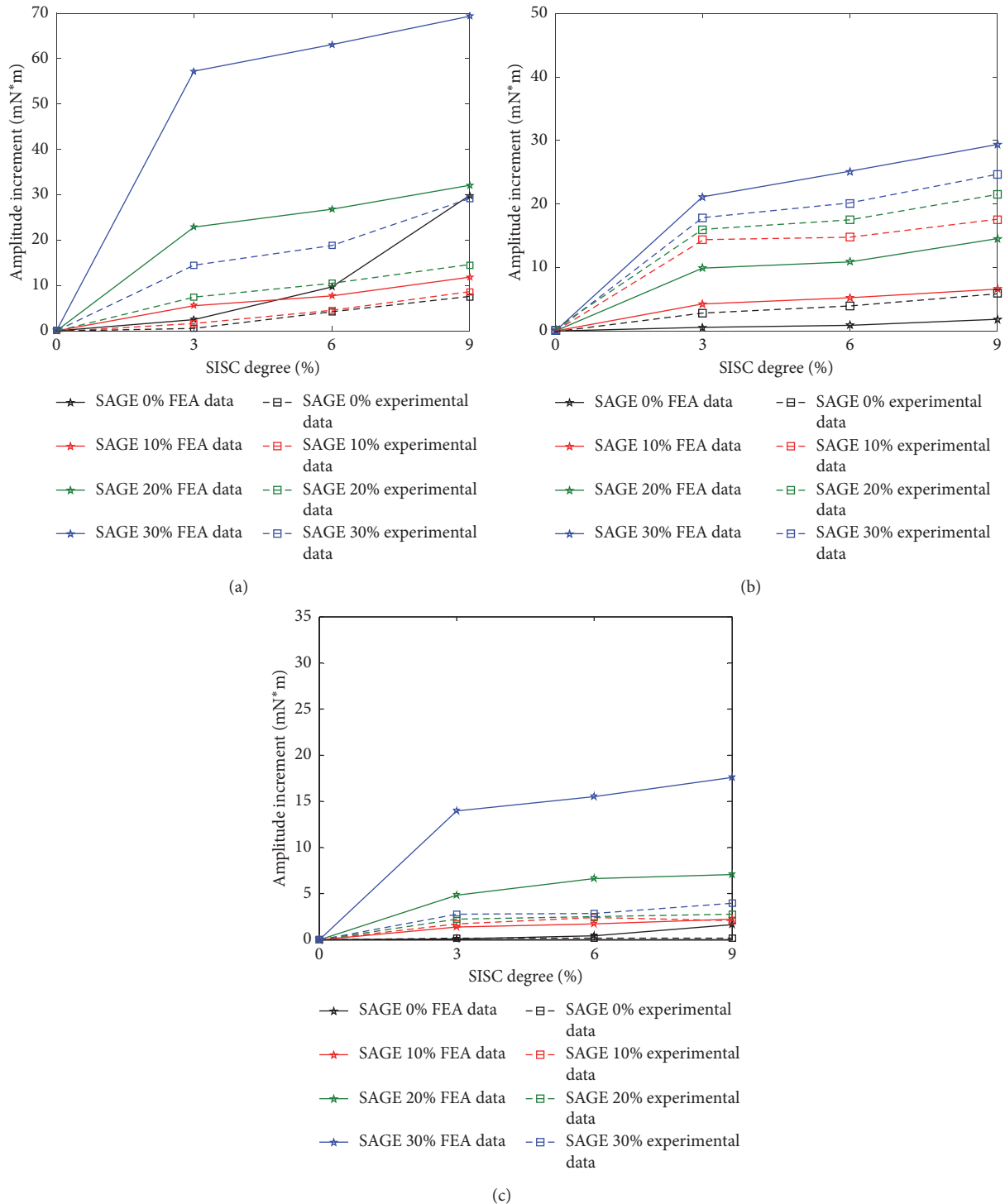
Figure 17: Impact comparison between CF and SISC faults: (a) 2nd harmonic, (b) 4th harmonic, and (c) 6th harmonic.

On the contrary, the comparison between the combined faults and the single SAGE faults indicated in Figure 17, where the curves marked with "SAGE 0%" denotes the single SISC fault, suggests that the combined faults generally have a more intensive sensitivity than the single SISC faults. Similarly, the comparison result illustrated in Figure 18 shows that the impact sensitivity of the combined faults is more intensive than that of the single SAGE faults (the single SAGE faults are the curves marked as "SISC 0%").

Based on the previous analysis, the final sensitivity rank order among the single and the combined faults should be: (1) the combined faults, (2) the single SISC fault, and (3) the single SAGE fault.
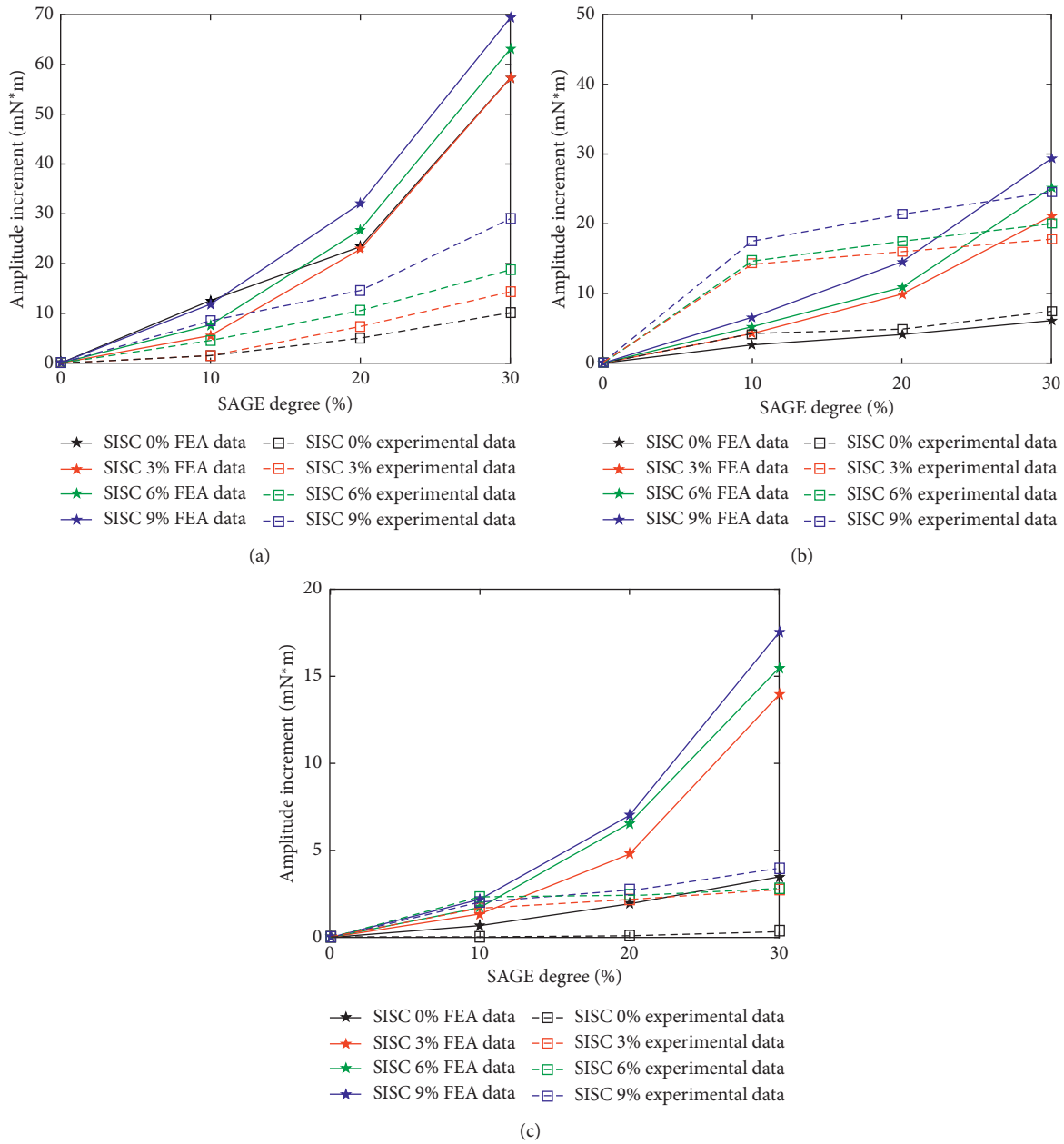
FIGURE 18: Impact comparison between CF and SAGE faults: (a) 2nd harmonic, (b) 4th harmonic, and (c) 6th harmonic.

4. Conclusions

In this paper, the EMT ripple characteristics in a synchronous generator caused by the single SAGE fault, the single SISC fault, and the combined fault composed of SAGE and SISC are analyzed and compared. The novelty of this paper primarily lies in the following three issues. (1) We investigate the EMT ripple properties not only under the single SAGE fault and the single SISC fault but also in the combined fault cases which are rarely taken into account by other studies. (2) We specifically design and manufacture a novel fault simulating generator which has been rarely reported and is able to simulate both the single and the combined faults composed of SAGE and SISC at the same time. Since it is

hard to sample the EMT data from the actual generator set, the experimental data by the newly designed generator can be used as a reference for further related research studies. (3) We found out the impact sensitivity rank among the single and the combined faults on the EMT ripples. This is of significance and is potentially beneficial for the further studies related to the single and the combined faults mentioned in this paper.

The key conclusions drawn from the theoretical derivation, the FEA calculation, and the experiments are as follows.

The detailed EMT expressions for both the single and the combined faults are derived based on the analysis of the magnetic flux density variation. It is shown that the

fundamental-frequency magnetomotive force will induce only the DC component in EMT in normal condition. However, the occurrence of SAGE will introduce the 2nd harmonic, while SISC fault will bring in both 2nd and 4th harmonics to EMT. Interestingly, the EMT characteristics of the combined faults are not the simple superposition of the two single faults. When the combined fault takes place, the new components include not only the 2nd and the 4th harmonics but also the 6th harmonic which is newly produced in addition to those induced by the two single faults. The more severe the fault degree is, the more the corresponding ripple amplitudes will be increased. Therefore, the harmonic component construction of the EMT can be employed as a tool for the identification and diagnosis among these three types of faults.

The finite element calculation and the experimental studies are carried out on the CS-5 prototype generator which is of two poles and 3000 rpm. This prototype generator is specifically designed and manufactured ourselves and is able to simulate both the single and the combined faults composed of SAGE and SISC. The FEA result as well as the experimental data generally follows the theoretical analysis conclusion. It is shown that the combined fault has the highest rank in the impact sensitivity on the EMT ripples, while following it is the single SISC fault. The single SAGE fault has the lightest impact on EMT among these three types of faults. This result is highly potential to be further applied in the future studies related to the mentioned faults in this paper.

The further work of this paper will lie in the EMT ripple restrain and the compensation method under the single and the combined faults composed of SAGE and SISC.

Abbreviation

EMT: Electromagnetic torque
CF: Combined fault
SAGE: Static air-gap eccentricity
SISC: Stator interturn short circuit
FEA: Finite element analysis
MFD: Magnetic flux density
MMF: Magnetomotive force
EMF: Electromotive force
PPUA: Permeance per unit area

Nomenclature

F_r, F_{r1+}:	Rotor MMF in normal condition and SISC case, respectively
F_s, F_{s1+}:	Stator MMF in normal condition and SISC case, respectively
ω:	Electrical angular frequency
t:	Time
α_m:	Mechanical circumferential angle
I_s:	Short circuit current
I_r:	Current in the remaining route of short circuit turns
I_{a1}, I_{a2}:	Branch current of phase A
Ψ:	Internal power angle of generator
F_d:	Pulsating MMF amplitude generated by SISC
F_{d+}, F_{d-}:	Forwardly and inversely rotating MMF amplitude
α_{sm}:	Angle of central position of short circuit turns
I_{f0}:	Exciting current produced by exciting system
I_{f2}:	Induced current in exciting windings by SISC
N:	Number of exciting turns per pole
Λ_0:	Normal PPUA
q:	Number of slots per pole per phase
w_c:	Number of turns in serial for each phase
k_{w1}:	Fundamental winding factor
τ:	Polar distance
f:	Fundamental electrical frequency
L:	Axial length of stator core
$F_{r1\rightarrow}$, F_{s1-}:	Inversely rotating rotor and stator MMFs at ω, respectively
F_{r3+}, F_{s3+}:	Inversely rotating rotor and stator MMFs at 3ω, respectively
W:	Magnetic energy in air gap
R_0:	Average radius of air gap
R_s:	Inner radius of stator core
R_r:	Outer radius of stator core
g_0:	Average length of radial air gap
μ_0:	Permeability of air
δ_s:	Relatively static air-gap eccentricity
ρ:	MMF proportion depending on SISC position
p:	Number of pole pairs
T, T_{Normal}, T_{SAGE}, T_{SISC}, T_{CF}:	EMT and EMT in normal, SAGE, SISC, and CF case, respectively
φ:	Power factor angle
z:	Winding reactance
P:	Output power of generator
U_a, U_b, U_c:	Three-phase voltages
I_a, I_b, I_c:	Three-phase currents.

Data Availability

The data used to support the findings of this study are available from the corresponding author upon request (wangxiaolong126.com).

Conflicts of Interest

The authors declare that they have no conflicts of interest regarding the publication of this paper.

Acknowledgments

References

[1] M. Rossander, A. Goude, and S. Eriksson, "Mechanical torque ripple from a passive diode rectifier in a 12 kW vertical Axis wind turbine," *IEEE Transactions on Energy Conversion*, vol. 32, no. 1, pp. 164–171, 2017.

[2] K. Tefera, P. Tripathy, and R. Adda, "Electromagnetic and mechanical stress analysis of wind-driven synchronous reluctance generator," *CES Transactions on Electrical Machines and Systems*, vol. 3, no. 1, pp. 107–114, 2019.

[3] T. Feehally, I. E. Damián, and J. M. Apsley, "Analysis of electromechanical interaction in aircraft generator systems," *IEEE Transactions on Industry Applications*, vol. 52, no. 5, pp. 4327–4336, 2016.

[4] J.-K. Park, C.-H. Kim, G.-J. Cho, S.-H. Sohn, and S.-J. Chung, "A novel reclosing algorithm considering turbine-generator shaft torque," *IEEE Transactions on Power Delivery*, vol. 32, no. 2, pp. 703–712, 2017.

[5] W. M. Lin, C. C. Tsai, and C. H. Lin, "Analysing the linear equivalent circuits of electromechanical systems for steam turbine generator units," *IET Generation, Transmission & Distribution*, vol. 5, no. 7, pp. 685–693, 2011.

[6] L. Hao, J. Wu, and Y. Zhou, "Theoretical analysis and calculation model of the electromagnetic torque of nonsalient-pole synchronous machines with interturn short circuit in field windings," *IEEE Transactions on Energy Conversion*, vol. 30, no. 1, pp. 110–121, 2015.

[7] X. Song, Y. Wang, D. Liu, S. Wang, and D. Liang, "Short-circuit characteristics of a high temperature superconducting wind turbine generator employing a segmented armature winding," *IEEE Transactions on Applied Superconductivity*, vol. 29, no. 5, pp. 1–5, 2019.

[8] Y.-L. He, W.-Q. Deng, G.-J. Tang, X.-L. Sheng, and S.-T. Wan, "Impact of different static air-gap eccentricity forms on rotor UMP of turbogenerator," *Mathematical Problems in Engineering*, vol. 2016, Article ID 5284815, 13 pages, 2016.

[9] Y.-L. He, W.-Q. Deng, B. Peng et al., "Stator vibration characteristic identification of turbo generator among single and composite faults composed of static air-gap eccentricity and rotor inter turn short circuit," *Shock and Vibration*, vol. 2016, Article ID 5971081, 14 pages, 2016.

[10] G.-J. Tang, M.-Q. Ke, Y.-L. He, and F.-L. Wang, "United electromagnetic characteristics and online monitoring method of static air-gap eccentricity of turbo-generator," *Journal of Electrical Engineering and Technology*, vol. 11, no. 6, pp. 1614–1627, 2016.

[11] T. Goktas, M. Zafarani, and B. Akin, "Discernment of broken magnet and static eccentricity faults in permanent magnet synchronous motors," *IEEE Transactions on Energy Conversion*, vol. 31, no. 2, pp. 578–587, 2016.

[12] W. Doorsamy, A. A.-E. Abdallh, W. A. Cronje, and L. Dupre, "An experimental design for static eccentricity detection in synchronous machines using a cramér-rao lower bound technique," *IEEE Transactions on Energy Conversion*, vol. 30, no. 1, pp. 254–261, 2015.

[13] C. Bruzzese, "Diagnosis of eccentric rotor in synchronous machines by analysis of split-phase currents-part I: theoretical analysis," *IEEE Transactions on Industrial Electronics*, vol. 61, no. 8, pp. 4193–4205, 2014.

[14] M. E. K. Oumaamar, Y. Maouche, M. Boucherma, and A. Khezzar, "Static air-gap eccentricity fault diagnosis using rotor slot harmonics in line neutral voltage of three-phase squirrel cage induction motor," *Mechanical Systems and Signal Processing*, vol. 84, pp. 584–597, 2017.

[15] S. Nadarajan, S. K. Panda, B. Bhangu, and A. K. Gupta, "Hybrid model for wound-rotor synchronous generator to detect and diagnose turn-to-turn short-circuit fault in stator windings," *In IEEE Transactions on Industrial Electronics*, vol. 62, no. 3, pp. 1888–1900, 2015.

[16] S. Moon, H. Jeong, H. Lee, and S. W. Kim, "Interturn short fault diagnosis in a PMSM by voltage and current residual analysis with the faulty winding model," *IEEE Transactions on Energy Conversion*, vol. 33, no. 1, pp. 190–198, 2018.

[17] K. N. Gyftakis and J. C. Kappatou, "The zero-sequence current as a generalized diagnostic mean in Δ-connected three-phase induction motors," *IEEE Transactions on Energy Conversion*, vol. 29, no. 1, pp. 138–148, 2014.

[18] H. Jeong, S. Moon, and S. W. Kim, "An early stage interturn fault diagnosis of PMSMs by using negative-sequence components," *IEEE Transactions on Industrial Electronics*, vol. 64, no. 7, pp. 5701–5708, 2017.

[19] L. Otava, "Implementation of PMSM inter-turn short fault detection using frequency analysis of stator currents," *IFAC-papers On Line*, vol. 49, no. 25, pp. 86–91, 2016.

[20] Y.-L. He, F.-L. Wang, G.-J. Tang, and M.-Q. Ke, "Analysis on steady-state electromagnetic characteristics and online monitoring method of stator inter-turn short circuit of turbo-generator," *Electric Power Components and Systems*, vol. 45, no. 2, pp. 198–210, 2017.

[21] S. E. Dallas, A. N. Safacas, and J. C. Kappatou, "Interturn stator faults analysis of a 200-MVA hydrogenerator during transient operation using FEM," *IEEE Transactions on Energy Conversion*, vol. 26, no. 4, pp. 1151–1160, 2011.

[22] Y. He, Y.-Y. Zhang, M.-X. Xu, X.-L. Wang, and J. Xiong, "A new hybrid model for electromechanical characteristic analysis under SISC in synchronous generators," *IEEE Transactions on Industrial Electronics*, vol. 67, no. 3, pp. 2348–2359, 2019.

[23] Y.-L. He, M.-Q. Ke, F.-L. Wang, G.-J. Tang, and S.-T. Wan, "Effect of static eccentricity and stator inter-turn short circuit composite fault on rotor vibration characteristics of generator," *Transactions of the Canadian Society for Mechanical Engineering*, vol. 39, no. 4, pp. 767–781, 2015.